PCCP

Accepted Manuscript

ROYAL SOCIETY OF CHEMISTRY

www.rsc.org/pccp

TOC Graphic

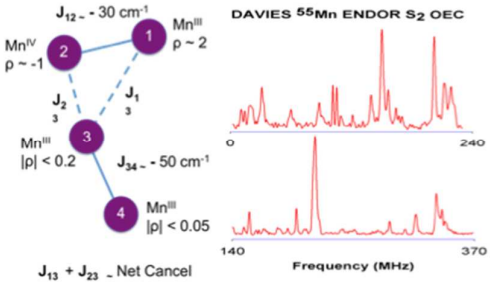

^{55}Mn pulsed ENDOR of the Oxygen Evolving Complex (S_2 state) at 2.5K indicates the presence of a $Mn^{III}_3Mn^{IV}$ tetranuclear cluster.

Cite this: DOI: 10.1039/c0xx00000x

www.rsc.org/xxxxxx

ARTICLE TYPE

Electronic Structure of the Oxygen Evolving Complex in Photosystem II, as revealed by ^{55}Mn Davies ENDOR Studies at 2.5 K.

Lu Jin,[a] Paul Smith,[a] Christopher J. Noble,[b] Rob Stranger,[a] Graeme R. Hanson[b*] and Ron J. Pace[a*]

Received (in XXX, XXX) Xth XXXXXXXXX 20XX, Accepted Xth XXXXXXXXX 20XX

DOI: 10.1039/b000000x

We report the first ^{55}Mn pulsed ENDOR studies on the S_2 state multiline spin ½ centre of the Oxygen Evolving Complex (OEC) in Photosystem II (PS II), at temperatures below 4.2 K. These were performed on highly active samples of spinach PS II core complexes, developed previously in our laboratories for photosystem spectroscopic use, at temperatures down to 2.5 K. Under these conditions, relaxation effects which have previously hindered observation of most of the manganese ENDOR resonances from the OEC coupled Mn cluster are suppressed. ^{55}Mn ENDOR hyperfine couplings ranging from ~ 50 to ~ 680 MHz are now seen on the S_2 state multiline EPR signal. These, together with complementary high resolution X-band CW EPR measurements and detailed simulations, reveal that at least two and probably three Mn hyperfine couplings with large anisotropy are seen, indicating that three Mn^{III} ions are likely present in the functional S_2 state of the enzyme. This suggests a low oxidation state paradigm for the OEC (mean Mn oxidation level 3.0 in the S_1 state) and unexpected Mn exchange coupling in the S_2 state, with two Mn ions nearly magnetically silent. Our results rationalize a number of previous ligand ESEEM/ENDOR studies and labelled water exchange experiments on the S_2 state of the photosystem, in a common picture which is closely consistent with recent photo-assembly (Kolling et al., *Biophys. J.* 2012, **103**, 313-322) and large scale computational studies on the OEC (Gatt et al., *Angew. Chem. Int. Ed.* 2012, **51**, 12025-12028, Kurashige et al. *Nature Chem.* 2013, **5**, 660-666).

Introduction

Photosystem II (PS II)[‡] in plants, algae and photo-synthetic bacteria oxidizes water within the Oxygen Evolving Complex (OEC), located near the photo-oxidizable reaction centre, P680.[1] The OEC consists of a redox accumulating Mn_4/Ca catalytic cluster which binds water and electrons pass from this cluster to $P680^+$ through an oxidizable tyrosine on the D1 peptide, Tyr_Z. The multi-nuclear Mn_4/Ca cluster proceeds through five intermediate 'S' states, four meta-stable (labelled S_0, S_1, S_2 and S_3) and one short-lived state, S_4 (subscripts indicate number of stored oxidizing equivalents). Water exchanges with the site up to S_3[2] and the oxidation of two water molecules to di-oxygen occurs in a concerted, four electron step. PS II is a membrane bound dimer[1] and atomic detail of the Mn_4/Ca catalytic site has recently been revealed by a 1.9 Å resolution crystal structure.[3] This and earlier lower resolution X-ray crystallographic structures,[4] correspond formally to the 'dark stable' S_1 state.

S_0 and S_2 have odd numbers of unpaired electrons, with net spin ½ ground states arising from a predominantly anti-ferromagnetic coupling of all four Mn ions.[5] They exhibit complex ^{55}Mn hyperfine structured continuous wave electron paramagnetic resonance (CW EPR) signals at low temperature (multiline (ML) signals), the S_2 ML being first reported by Dismukes.[6] Photo-assembly[7] and Mn X-ray Absorption Near Edge Structure (XANES) measurements[8,9] show the mean Mn oxidation states in the functional cluster to be significantly higher than II. Thus S_1 is either Mn^{III}_4 or $Mn^{III}_2Mn^{IV}_2$, (or equivalent combinations). Spectroscopic data (but not EPR) bearing upon these 'low and high' oxidation state paradigms have been recently reviewed.[10] In the low and high oxidation state paradigms, S_2 is $Mn^{III}_3Mn^{IV}$ or $Mn^{III}Mn^{IV}_3$, respectively. Since the mechanism of water oxidation in the OEC is yet undetermined, resolution of the actual Mn oxidation states will be crucial in defining reaction pathway possibilities.[11]

The S_2 ML EPR spectrum contains 18-20 resolved hyperfine resonances, centred close to g = 2.00, with little g anisotropy and is at least 180 mT (i.e. ~ 5,000 MHz) wide at X-band frequencies (one resonance is typically obscured by the narrow Tyr_D radical signal near g = 2.00[5]). It may be generated by continuous illumination at low temperature (~ 200 K) with visible (e.g. green) light. The signal resembles the 'classic' 16 hyperfine line EPR signals seen in anti-ferromagnetically coupled Mn^{III} /Mn^{IV} oxo bridged dimers below ~ 20 K.[12,13] These signals are generally < 130 mT wide, significantly narrower than the S_2 ML and have fewer resonances. However the S_2 ML EPR spectrum is narrower, with fewer resonances, than the only example of an authentic Mn^{III} /Mn^{IV}_3 net spin ½ tetramer (~ 26 resonances, ~ 195 mT).[14]

Two approaches exist to modelling the magnetic coupling and Mn hyperfine interactions of the S_2 state within the OEC cluster; (i) the Mn tetramer model or (ii) the effective dimer (or 'near dimer') model in which only two Mn ions dominate the hyperfine spectrum.

In 2002 Dismukes et al. provided a rationalisation of the EPR, ENDOR and X-ray absorption spectroscopic data for the S_2 state which were consistent with a tetrameric magnetic organisation of the four Mn ions in the OEC[15]. This was also supported by the early, low resolution X-ray diffraction data on PS II which was beginning to emerge[4d,e]. In addition, the CW EPR and pulsed ^{55}Mn ENDOR data on the S_2 ML signal reported by Britt et al. in 2000[18b] were suggestive of a '3 +1' organisation of the OEC cluster, with three Mn ions strongly internally exchange coupled, with variable coupling to a fourth 'dangler' Mn ion. Dismukes et al. considered a number of coupling modes ('butterfly, Y shaped' etc.) between the four Mn ions, for which an oxidation state organisation of $Mn^{III}_3Mn^{IV}$ was favoured for S_2. Different combinations of internal inter-ion exchange couplings were shown to be consistent with net spin ½ or higher spin ground states, well known to be observable in S_2 under appropriate experimental conditions (see discussions in refs, 5, 15 for details). In these and the modelling of Britt et al., the native S_2 ML was inferred to arise form a configuration in which substantial hyperfine couplings were contributed by each of the four Mn in the coupled cluster. Interestingly however, Dismukes et al. proposed that a known, reduced spin ½ cluster state, (NO-reduced, probably equivalent to S_0 in overall oxidation state, see ref. 15) was effectively 'dimer like', with two Mn internally coupled silent. However tetramer pictures have largely dominated interpretation of the OEC magnetic spectroscopy ever since and indeed the PS II crystal structures, at increasing resolution, gave general support to the idea.

Two dimer or near dimer models have been suggested[16,17] and both require a means to increase the spectral width expected from conventional Mn^{III} and Mn^{IV} hyperfine parameters, to give a pattern > 170 mT wide. A large, rhombic anisotropic Mn^{III} hyperfine tensor, with a substantial quadrupolar interaction, was assumed in the pure dimer model (remaining Mn coupled silent).[16] Bonvoisin et al.[17] assumed all the Mn hyperfine tensors were isotropic, with two contributing ~ 2/3 of the pattern width (ie near dimer) and one other being small. The crystallographic structures of PS II show all OEC Mn ions are close enough (with oxo, carboxylato bridging) for the presence of significant exchange coupling, which has been confirmed through computational chemistry calculations.[10]

Recently we computationally examined the ground S_2 spin ½ state[10], using OEC models based on the then available[4] XRD data and using multiple single determinant DFT calculations. This showed that it was possible, under some circumstances, for the tetra-nuclear cluster to magnetically couple in near dimer like fashion, internally. This involved two Mn (in states III and IV) combining with net spin ½ and large effective hyperfine couplings, while the other two Mn ions (both III or IV) couple to be largely 'silent' (ie. net anti-ferromagnetic, spin ~ 0). Net coupling between these Mn pairs was weak. Now, detailed high level calculations on the OEC have appeared[19], using multi-dimensional quantum entanglement techniques and employing the most recent OEC XRD structure[3]. These predict something quantitatively similar for the coupling within the OEC (see Discussion below). In both cases some small, or near cancelling Mn-Mn exchange interactions occur. Earlier tetramer[15,18b] models however generally predicted effective hyperfine contributions for all Mn ions to have isolated ion values or greater (for one Mn^{III}). The dimer like models require one hyperfine interaction to be in the isolated ion range (~ 200 - 300 MHz), one about twice this, as well as interactions below ~ 100 MHz, to give an S_2 ML pattern of ~ 190 mT width (~ 5.4 GHz).

^{55}Mn electron nuclear double resonance (ENDOR) measurements on the S_2 ML CW EPR signal should reveal the individual hyperfine frequencies directly. Several groups have performed such studies (plant, cyanobacterial PS II) at 4.2 K and hyperfine couplings from ~ 170 - 340 MHz were seen in a broad envelope of somewhat variable shape, with a maximum of ~ 240-280 MHz.[18,20-25] In these no resonances from couplings above 400 MHz or below ~ 160 MHz have been reported, but couplings above 400 MHz have been observed†† in plant PS II. We address this further in ESI Section ES6.

All ENDOR spectra are sensitive to nuclear spin relaxation to some degree. Pulsed techniques, (e.g. Davies ENDOR) require the nuclear T_1T_2 product to be sufficiently long for coherent magnetization rotation during the RF pulses.[26] In paramagnetic systems at cryogenic temperatures, these rates depend strongly on the electron spin coupling to the nucleus through hyperfine fields experiencing time dependent, matrix phonon induced modulation etc. These effects may have non straight forward consequences near 0K. T_1 typically drops rapidly with increasing temperature (rates increase), but rotating frame T_2 rates can still remain relatively insensitive to temperature (and be high, ie short T_2), as these are strongly influenced by very low frequency phonon modes (dominant at lowest temperatures). Then they cause nuclear magnetisation dephasing in the rotating (x, y) frame, with loss of ENDOR intensity[26] In general however ENDOR detectability should improve with decreasing temperature. Thus, nuclear spin relaxation may have hindered previous detection of some ENDOR transitions in the S_2 state of the tetra-nuclear Mn cluster (particularly from Mn^{III} ions, see Discussion), as all previous ^{55}Mn ENDOR studies have been performed at 4.2 K.

In addition, Davies ENDOR does not generally yield absolute signal intensities as the output (B_2) from the radio-frequency (RF) synthesizer may vary dramatically as a function of frequency (1-400 MHz, particularly at high frequencies). This means that the *total number* of nuclear transitions contributing to a particular ENDOR resonance frequency region is not known. Thus the presence of partially resolved structure on the ENDOR signals seen and the absence of couplings outside 170 -340 MHz, suggested then that three nearly equivalent isotropic Mn couplings (~230 MHz and approximately overlapping in the spectra) and one axial anisotropic coupling with a perpendicular component ~ 350 MHz were present[19-25]. The latter was assigned to a single Mn^{III} and the former to three Mn^{IV} ions in the high oxidation state models mostly used by these workers in detailed spectral interpretation.

Herein we report the first such studies at temperatures down to

2.5 K, together with complementary CW EPR studies at X- band frequencies. ^{55}Mn hyperfine interactions ranging from ~ 50 to ~ 680 MHz are now seen on the S_2 state ML signal. At least two and probably three interactions of large hyperfine anisotropy are present (i.e. Mn^{III}, due to Jahn Teller effects), suggesting the S_2 state is indeed $Mn^{III}{}_3Mn^{IV}$, consistent with the low oxidation state paradigm.

Importantly, these new findings utilize highly active plant PS II core complex preparations, specifically developed by us previously for spectroscopic studies[27] which have already revealed new details of the P680 reaction centre.[28]

Experimental Methods

PSII sample preparation and illumination treatment

PSII membrane and core samples were prepared from market spinach (*Synechococcus oleracia)* essentially as per Smith et al.,[27] with some modifications. 7.0 g of Poros HQ 20 Anion exchange media was packed into a Waters AP 10 glass column to a pressure of 200 PSI. PS II, solubilized, with up to 80 mg chlorophyll total content, was loaded onto the column. Eluted PS II cores comprised of 4 - 5 % of the total chlorophyll loaded. Column pressure was operated below 300 PSI. Eluent volumes with A_{470} above 1.0 OD were pooled and concentrated using centrifugal concentrators with a 10 kDa cut-off membrane. Final volumes were 0.7 ml of concentrated Core complex solution. ENDOR samples had Chl concentrations of 5 -7 g/l with a chl a / b ratio above 16. Oxygen evolution was measured using a Clarke type electrode with p-Phenylbenzoquinone (PpBQ) as the added electron acceptor. Samples were selected with a minimum VO_2 of 3000 µmol O_2 / mg chl. / hr. These activity levels are the highest yet reported in plant PS II core material and comparable to those obtained from thermophylic bacterial PS II[27]

PSII core samples for ENDOR (stored in darkness at -80 ^{o}C) were thawed on ice water in darkness and 250 µl aliquots were loaded into 3.0 mm ID quartz EPR tubes (Wilmad 707 SQ) and pre-illuminated (15 seconds) at 240 K. Samples were then annealed for ~30 minutes on ice water in total darkness to restore the S_1 state. S_1 to S_2 turnover occurred at 240 K, using a 250 W projector lamp, with a narrow window green filter. Samples were then frozen in liquid N_2 and were inserted into the EPR cavity within 20 minutes of illumination. For X band CW EPR measurements, samples were loaded into 4 mm OD EPR tubes without any additions and the S_1 state to S_2 state turnover occurred as above. PS II membrane samples for CW EPR were similarly treated, but the effective OEC concentration was ~ 30 µM.

X -Band CW EPR

X-band CW EPR measurements were performed at 6.5 K using a Bruker Biospin Elexsys E500 spectrometer with a Bruker SHQX resonant cavity, fitted with an Oxford Instruments ESR900 helium flow cryostat in conjunction with an Oxford ITC4 temperature controller. Spectrometer frequency; 9.377 GHz, microwave power; 0.5 mW and modulation amplitude; 10 mT. The magnetic field was calibrated with a Bruker ER035M NMR Gaussmeter.

X- Band Pulsed EPR and ENDOR

Pulsed EPR and ENDOR experiments were performed at the Centre for Advanced Imaging, The University of Queensland, using a Bruker Biopsin Elexsys E580 Pulsed EPR/ENDOR spectrometer fitted with an Oxford Instruments CF935LT helium cryostat. Temperatures below 4 K (down to ~ 2.5 K) were achieved by reducing the partial pressure (measured with a capacitance manometer and an Infinicon CC3 gauge) of liquid He by pumping (40 l /min Leybold roughing pump) on the liquid He. The temperature was controlled using an Oxford Instruments ITC 503 temperature controller in conjunction with the transfer arm needle valve and valves on the side arm of the cryostat and between the cryostat and the roughing pump. The X- and Q-band spectrometer system employed an X-band ER4118XMD-4W1 ENDOR resonator, a DICE I ENDOR unit with an Amplifier Research 1-400 MHz RF amplifier (150A400), a Bruker frequency counter and a Bruker ER036TM teslameter for calibrating the microwave frequency and magnetic field, respectively.

Electron spin echo-detected (ESE) field-swept spectra were routinely measured using the pulse sequence: $\pi/2$-τ-π-τ-echo, where π = 32 ns and τ = 200 ns to ensure measurement of either the S_2 ML state species or the background Mn^{II} species. From these spectra appropriate resonant field positions were identified and ^{55}Mn-Davies stochastic ENDOR spectra were measured with the pulse sequence: π-π(RF)-T-$\pi/2$-τ-π-τ-echo within two RF ranges (1-230 and 140-370 MHz, after output frequency doubling, (see below), with timings: π = 24 ns, τ = 200 ns, π(RF) = 6 µs and a delay T = 600 ns. Typically 1500 scans were acquired per experimental run (~ 60 hours).

The Bruker Biospin DICE I has a bandwidth of 200 MHz and the radiofrequency magnetic field strength (B_2) output profile over 1-200 MHz is not linear, peaking around 14-20 MHz. Data were able to be collected up to 400 MHz using a frequency doubler (15542, Mini-circuits). At higher RF frequencies (140-370 MHz), the B_2 output from the DICE I unit was significantly attenuated. Consequently, the RF output from the frequency doubler was amplified using a BLAXXS300RS amplifier (from a Bruker NMR spectrometer) and then attenuated so as to not damage the 150 W Amplifier Research (AR) RF amplifier. A Tenuline coaxial attenuator (Model 8325, 30 db) was used for both low and high frequency regions and an additional 10 db attenuation was added for the low frequency region. The inability to achieve a flat B_2 profile from the DICE I unit during a stochastic ENDOR experiment prevents (i) spin quantitation and (ii) the use of transition intensities from orientation selective experiments.

X- Band T_1 Relaxation Measurements

Spin lattice relaxation times, T_1, were measured using an inversion recovery pulse sequence on the Bruker Biospin Elexsys E580 pulse EPR spectrometer at the temperatures and field positions specified in the text. The pulse sequence used was: π(Inv) - T - $\pi/2$ - τ - π - τ - echo with timings: π(Inv) = 26 ns, π = 32 ns, T = 500 ns, τ = 200 ns.

X-Band CW-EPR and ^{55}Mn-ENDOR Simulations

The S_2 state X-Band CW-EPR and ^{55}Mn-ENDOR spectra were simulated interactively, to maintain consistency. Essentially the same spin Hamiltonian (Eq. 3) was used for both simulations,

which assumed that the effective spin of the ground state is S_{eff} = 1/2. For the S_2 state ML simulations, the three-Mn system was treated using the complete matrix diagonalization method. For the four-Mn system the matrix approach was prohibitive computationally and this system was treated using second order perturbation theory. Spectral simulations were performed using the EasySpin package in MATLAB.[29]

DFT Calculation Details

DFT calculations were performed as described previously[30,31] using the ADF program, to obtain initial values of the spin Hamiltonian parameters. Only Euler angles of the hyperfine matrices on each Mn were taken from the simulations and used as inputs for subsequent refinement. All calculated structures were optimized without restrictions, using the BP86 functional and TZP basis sets for all atoms. Geometries from the 'Berlin' (Type I) and 'Hyogo' (Type II) isolated clusters were used. [30,31]

Results

X- Band CW EPR Spectroscopy

It is known that several factors (PS II species/preparation, cryoprotectant, small alcohols at < 1M concentration etc.) subtly influence the detailed, hyperfine structure of the S_2 ML CW EPR spectrum in functional PS II [5,32]. A possible basis for this structural 'flexibility' is seen computationally [30,31]. So called, 'broad' and 'narrow' (or sharper) forms[5] exist; narrow in cyanobacterial PS II and plant PS II membranes with MeOH, broad in the latter with EtOH (as in the first ML ENDOR studies[18a]) and in our plant PS II core complexes (below). Since the core complexes allow very high (> 200 µM) reaction centre concentrations, vital for ENDOR study, we focus on these principally here, but some results from membrane PS II are also presented.

Fig. 1A shows $S_2 - S_1$ (annealed) CW EPR difference spectra (Experimental Methods) of PS II core complexes and PS II membrane particles, both from higher plants. The core complex OEC concentration is approximately seven times higher than in the membrane samples. Although with glycerol cryoprotectant, the membrane spectrum is essentially the same as that seen for plant PS II in the presence of MeOH.[5] The core complex spectrum is very similar to that of membrane PS II in the presence of EtOH, the most 'pure' broad form observed by us,[5] although no mono-alcohol species are present in the PS II core samples. The spectra (Fig. 1) have virtually identical resonant field positions for the main hyperfine resonances, but differ in the detailed splitting on these resonances in the high resolution CW EPR spectra (Fig. 1B), particularly above g = 2. This is clearly not an intrinsic line-width effect and must arise from an anisotropic hyperfine interaction, as it is not seen fully on all of the main resonances (roughly every second resonance in the 300-400 mT region). The hyperfine coupling is of the order of 80 MHz (i.e. ~3 mT) in the broad form which is reduced to ~ 50 MHz (~ 2 mT) in the narrow form. A hyperfine interaction of this magnitude is inconsistent with all previous high oxidation state modelling of the tetra-nuclear Mn cluster.

X Band Pulsed EPR Spectroscopy

The S_2 and S_1 states of the PS II core complexes were studied by pulsed EPR, with S_1 formed by S_2 state dark relaxation (30 min, 0 °C). The non OEC paramagnetic centres (cyt b559, Tyr_D radical, Q_a^- centre[1]) formed and trapped during S_2 state generation are largely unaltered by this dark annealing. Examples of echo detected field swept spectra are given in Fig. 2. The S_2 state spectrum shows six small sharp features from magnetically isolated Mn^{II}, typically found in these samples (< 2% of reaction centres). It is likely, they are of similar origin to the Mn^{II} seen in Sr substituted cynanobacterial PS II[23] and is probably OEC associated ('fades' variably with annealing). These sharp Mn^{II} positions were avoided in ENDOR measurements (below). The $S_2 \rightarrow S_1$ conversion kinetics were found to be somewhat sample dependent, which might reflect the fact that the core complex S_2 states as prepared are probably still heterogeneous in some property, which is reflected in the electron spin lattice relaxation rates (below).

Cox et al.[24] have determined electron spin lattice relaxation times (T_1) of the tetra-nuclear Mn cluster in the S_2 state as a function of temperature (~6–4.2 K.) and sample treatment (± MeOH) for PS II from spinach membranes and thermophilic

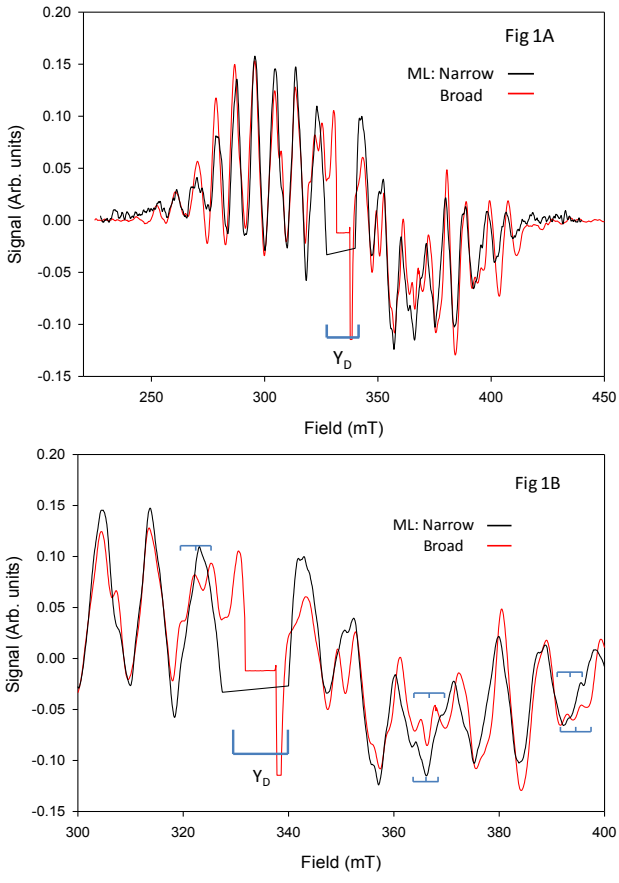

Figure 1 A: X Band CW EPR difference ($S_2 - S_1$) spectra of typical Multiline forms of the 'broad' (red, PS II Cores) and 'narrow' (black, PS II Membranes) types. Central region (indicated) about g = 2 is obscured by Tyr_D subtraction artifact. **B**: Expansion of (A) between 300-400 mT. Stick spectra (blue) reveal several examples of similarly patterned peak splittings. Spectrometer conditions are given in Experimental Methods.

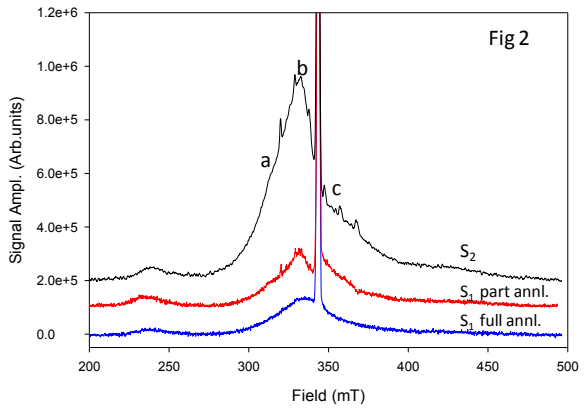

Figure 2. Echo detected field swept spectra of PS II Cores. Freshly illuminated S_2 (black), partially annealed S_1 (~ 20 min dark, 0 °C, red) and fully annealed S_1 (>30 min dark, 0 °C, blue) All spectra aligned at common g =2.000 at ν=9.634 GHz. Three field positions (g ~ 2.18 **a**, 2.05 **b** and 1.93 **c**) are shown on the S_2 state spectrum at which ENDOR measurements were made (see text). Oxidized cyt b_{559} is also present in these samples, (g_x ~ 2.9 resonance around 235 mT), as is the radical signal from oxidized Tyr_D near g = 2.00. The six small sharp features arise from Mn^{II} (see text).

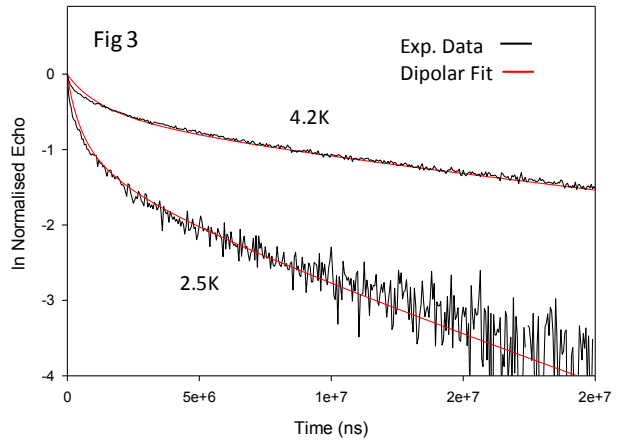

Figure 3: Saturation recovery (echo inversion recovery) T_1 plots for the S_2 ML signal (measured near point b in Fig. 2) at temperatures 2.5 K and 5.2 K. Plotted is ln ($\log_e$) normalized amplitude vs. time. At long times plots are linear (single exponential decay) but multi-exponential at short times. Fits (red) are to a mixed dipolar model (see text), with F parameter = 0.60, 2.5 K and F = 0.87, 5.2 K (see ESI Section ES1)

cyanobacteria. MeOH has a much greater influence on the T_1's (presumed averages from bi-exponential fits,[23] see also below) in plant, compared to cyanobacterial PS II. We have performed similar measurements on spinach cores, at 5.2 and 2.5 K (Fig. 3). At both temperatures the decay is a single exponential at long times, but faster and more complex at short times. We have previously shown that a 'mixed dipolar' model provides excellent fits to the S_0 and S_2 state multiline ESEEM envelope decays (dynamic $1/T_2$,) as well as $1/T_1$ rates for species near the OEC like Tyr_D,[33] (ESI Section ES1). This model assumes a fraction (F) of centres relax with a background plus dipolar (non exponential) rate, while the remainder relax with the background rate. Formally, this means a paramagnetic centre of short T_1, interacts through space with the paramagnet of interest (e.g. ML, centre, etc.). If the fast species is effectively even spin, it might be difficult to detect in conventional CW EPR. While this model cannot exactly describe relaxation pathways within the coupled Mn cluster, a basis for its approximate validity will emerge below. To compare with other data, we report fast and slow component rate estimates for two exponential fits and an exponential average $1/T_1$ relaxation rate for our samples, defined by:

$$1/T_{1AV} = \int_0^\infty Sig(t)\ dt \qquad (1)$$

where Sig(t) is the (normalized to unity at t = 0) longitudinal echo amplitude decay.

A comparison (Fig. 4) of the data from Cox et al.[24] with our results (Fig. 3) reveals that the weak temperature dependence seen for spinach PS II without MeOH is similar to that in both components of our spinach core complexes, Thus the $1/T_1$ rate depends weakly on temperature in the broad forms of plant PS II (core complexes and membranes without MeOH), while it has a strong dependence in the +MeOH narrow form, similar to that seen in cyanobacterial PS II (± MeOH). The S_2 ^{55}Mn ENDOR spectra of Cox et al.[24] also show a significant influence of MeOH for spinach PS II, but not cyanobacterial PS II. Thus the MeOH induced structural modifications in plant PS II, appear 'already in place' in cyanobacterial PS II. This is consistent with the known functional insensitivity of PS II to MeOH at ~ 1 M solvent concentrations. We will not explore this further here, but note from Fig. 4 that our electron $1/T_1$ rates at 2.5 K are ~ 10 times or more slower than have likely prevailed in *any* previous ^{55}Mn ENDOR measurements on the S_2 ML signal. The significance of this emerges below.

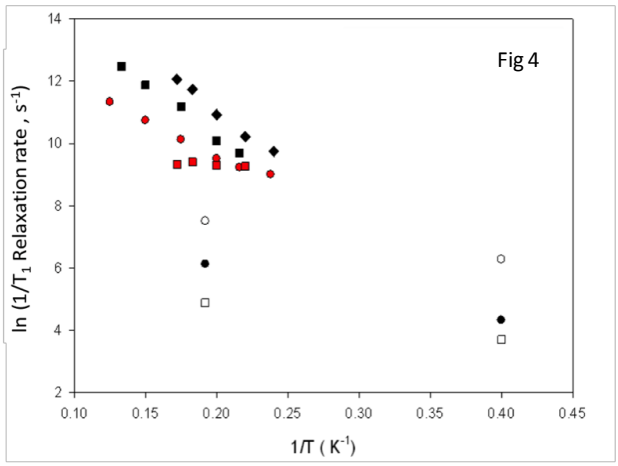

Figure 4: Temperature dependence of mean electron $1/T_1$ rates (s^{-1}) of the S_2 ML for different species/solvent conditions. Data on *S. Elongatus* and spinach (membranes) were taken from Cox et al.[24] Spinach core data (ESI Section ES1) plotted as the mean $1/T_1$ rate (see text) and fast and slow rates from two exponential fits. ● *S. Elongatus*, ■ *S. Elongatus* with added MeOH, ■ Spinach membranes, ◆ Spinach membranes with added MeOH, □ Spinach Core samples – slow component, ○ Spinach Core samples – fast component, ● Spinach Core samples – average rate.

X -Band Davies ENDOR Spectroscopy

^{55}Mn ENDOR measurements were made at 2.5 K, with some data at 4.2 K, to compare with earlier results of others. The 0-400

MHz frequency interval used should access all Mn couplings likely for dimer or tetramer OEC models. In first order, a coupling of A MHz gives ENDOR frequencies at ~ A/2 MHz, for this spin ½ system with nuclear hyperfine strongly dominating nuclear Zeeman and quadrupole terms. Experimental factors relevant for Davies (^{55}Mn) ENDOR with a system like the OEC include:[26]

1. The B_2 profile across the RF radiation frequency range.
2. The nuclear hyperfine value itself (roughly its isotropic value, A_{iso})
3. Hyperfine orientation selection at the envelope position where the pulsed ENDOR experiment is performed.

While the RF frequency is randomly varied to prevent heating artifacts (Experimental Methods), the B_2 value is not separately controllable (other than preset attenuation of the instrument dependent profile). The B_2 and hyperfine A_{iso} values determine the nuclear nutation 'flip angle' for a given RF pulse length.[26] This strongly influences the intensity of the ENDOR response when, as here, the hyperfine frequencies are much larger than the nuclear Zeeman frequencies (by factors of 10-100 at X- Band). Point 3 is crucial when large, anisotropic hyperfine components are present. Then the narrow electron spin packets (here ~ 10 MHz wide), excited at a particular magnetic field position of the ENDOR experiment do not sample equally the full powder pattern range of these hyperfine components. Particular molecular orientations are then selectively seen (or enhanced), influencing the observed intensities of ENDOR lines in non obvious ways. We return to this below in Data Analysis.

To (partially) address points 1 and 2, the RF acquisition range was divided into two overlapping segments, 0 - 230 MHz ('low frequency') and 140 - 370 MHz ('high frequency'), with 10 dB power attenuation applied in the low frequency measurements. Some Orientation selection, as in point 3, is inescapable even in simpler systems, (e.g. Mn^{III-IV} dimers), where largely non-overlapping transitions near the pattern edges may be resolved.[18,20] In these Mn^{III-IV} dimers the ENDOR spectrum is readily interpreted.[§] This is impractical here as the S_2 ML CW EPR spectrum has too many overlapping resonances across the envelope and is very indistinct and of low intensity near the edges. Consequently, we obtained ENDOR spectra around regions a, b and c in Fig. 2. Typical data, for the low frequency region are shown in Fig. 5A, with high frequency data from point b in Fig. 5B.

The OEC ^{55}Mn ENDOR spectra in Fig. 5 are far sharper, with more resolved detail than any previously reported. Resonances are seen across the full frequency range sampled, including features derived from magnetically isolated Mn^{II}. These occur as sharp peaks at well known positions around 105 MHz and 153-157 MHz ($M_s = \pm ½$) and at ~ 340 MHz ($M_s = 3/2$).[23,34] Weaker transitions are sometimes seen (depending on RF power) at half these frequencies, from harmonics generated by the RF frequency doubler. The relative intensities of some features vary significantly with magnetic field position, but all seem to be substantially present in spectra from the envelope peak, where most measurements were made (point *b* region, shows combination of several typical data sets). The results contrast sharply with previously reported ^{55}Mn ENDOR data from the ML centre[18,20-25] (Fig. 6), which mostly show only broad, partially structured resonances between ~ 85- 170 MHz (at X or Q band) with little dependence on the field sampling position. Our data typically exhibit some baseline slope or weak, very broad features (may be real, see below), but we are not confident of observing these reliably. Therefore the data have been digitally levelled where necessary (linear baseline corrections, ESI Sections ES4,ES5).

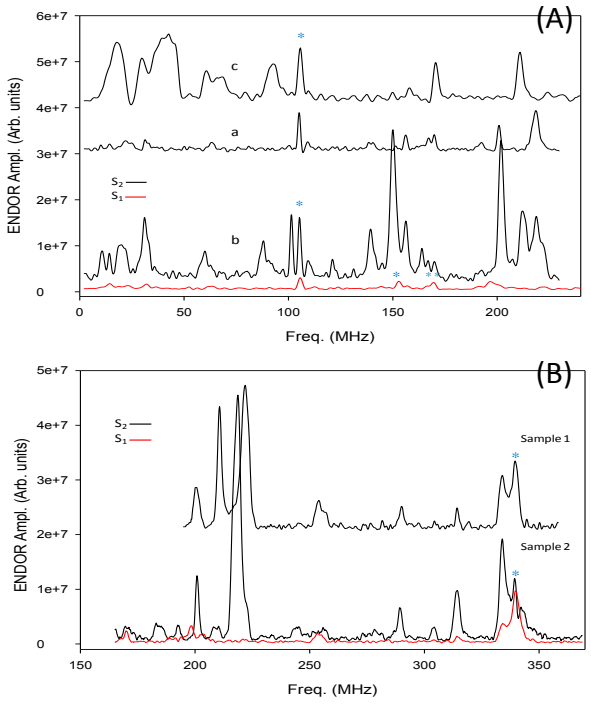

Figure 5. ^{55}Mn Davies ENDOR spectra of the S_2 state of PS II core samples at 2.5 K. (A) Low frequency region (0-240 MHz range), from points a, b, c on the S_2 ML envelope (Fig. 2, normalized to equal scan numbers). Point b spectrum is a combination of several data sets (same or different samples, see discussion in text, Fig. 5B), all taken at nominally same g value (2.05 ± 0.01), within an effective field range of < 3 mT and with 10 dB RF attenuation (Experimental Methods). Red spectrum is from point b for annealed S_1. Single starred peaks are from $M_I = \pm ½$ related Mn^{II} transitions and doubled starred peak is a 1st harmonic peak from the $M_I = 3/2$ related transition at ~ 340 MHz (see text , Fig. 5B). Transitions in the ~ 10 - 20 MHz region are expected from protons coupled to the S_2 ML centre (see text). (B) High frequency region (150-350 MHz) of representative samples, taken at point b on the S_2 ML envelope (0 dB RF attenuation). Red spectrum is from annealed S_1. Variation in the individual positions, intensities, of the strong transitions in the ~ 200-230 MHz range between samples is evident (see Discussion).

Fig. 5A clearly shows several small, likely anisotropic Mn hyperfine couplings (~ 40 - 120 MHz). From the total S_2 ML EPR spectral width, large couplings must then be present (see Discussion). Fig. 5B reveals these as resonances between 200 - 340 MHz, arising mostly from the S_2 state, with only Mn^{II} features being significantly present in the S_1 state samples. The sharp multiple peaks around 200 MHz and 300 MHz are unlike

anything previously reported for the ML ENDOR. Since they occur in groups, with variable intensity but roughly equal spacing within each group (~10 MHz near 200 MHz and ~ 15 MHz near 300 MHz), they likely arise from quadrupole transitions, presumably from the lower and upper edges respectively of a single large, highly anisotropic Mn hyperfine tensor, whose central component is responsible for the weak transitions around 250 MHz. We return to this in detail within the Data Analysis section below. The transition intensities near 200 MHz depend sensitively on field acquisition value, as the two spectra in Fig. 5B were taken (on separate samples) at similar field points in the *b* region (cf. the behaviour of these peaks in Fig. 5A). This was also seen in low frequency measurements in the *b* region (ESI Fig. S1), so must arise from closely spaced (< 1 mT) hyperfine determined positions in the ML envelope, which our sample/measurement conditions do not significantly broaden or smear. The narrow (~ 10 MHz) intrinsic linewidth (see below) of the ENDOR resonances contributes to this effect.

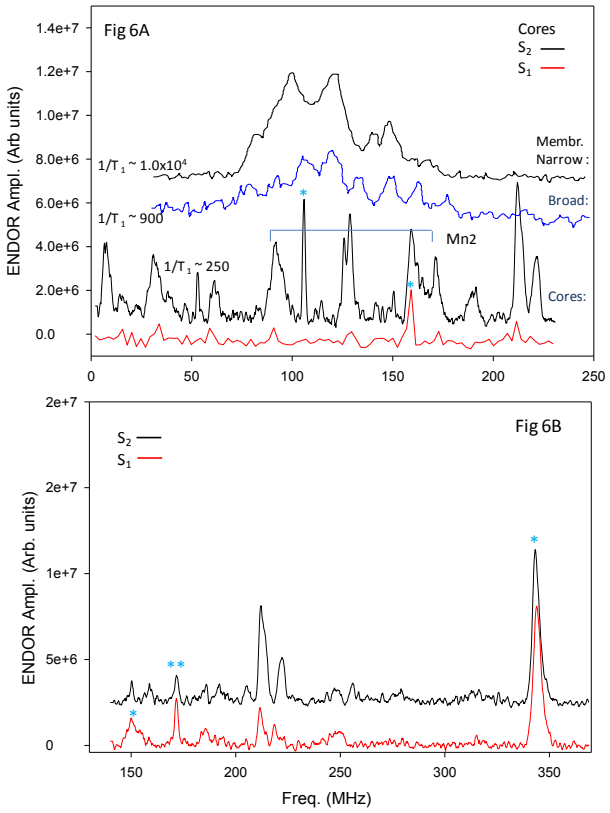

Figure 6. ^{55}Mn Davies ENDOR spectra of the S_2 state of PS II at 4.2 K and at point b on the ML envelope (Fig2). **A**: Low frequency region (1 - 230 MHz). RF attenuation, 10 dB (Experimental Methods). Red spectrum is from point b on annealed S_1 sample. Blue stick spectra corresponds to the Mn2 hyperfine range (as determined here, see text). Reproduced are the corresponding X band ML ENDOR spectra from PS II membranes (+MeOH, narrow form, Messinger, Lubitz et al.[22] and + EtOH, broad form (Britt et al.[18a]), both at 4.2 K. The electron relaxation rates ($1/T_1$, s^{-1}) at the ENDOR measurement temperatures are also indicated (Fig. 4).[35] For core complexes at 2.5 K, the average rate is ~ 90 s^{-1} (Fig. 4). **B**: High frequency region (140 -370 MHz) ^{55}Mn ENDOR spectra, acquired at 4.2 K at same point b on the ML envelope (0 dB RF attenuation). Red spectrum is from annealed S_1. Starred peaks at 170, 340 MHz are from Mn^{II}.

We see several S_2 related ENDOR peaks in the 90-170 MHz region (where previous work located broader resonances), but these clearly do not arise from near isotropic species nor totally dominate the ENDOR spectra. To test if this is nuclear relaxation related, experiments on our PS II Core samples were made at a higher temperature (4.2 K, Fig 6). Resonances in the 90-170 MHz region are now more pronounced, while those around 200-220 MHz diminish and essentially nothing beyond the Mn^{II} feature is seen at higher frequencies. The observed ENDOR transition line widths, either for the OEC resonances or the background Mn^{II} resonances are relatively narrow but not particularly temperature dependent, indicating, that they are dictated (over this temperature interval) mainly by inhomogeneous broadening ('static' effects). This is common in cryogenic EPR. Rather, elevating the temperature diminishes the *intensity* of OEC related resonances outside the 90-170 MHz region. This does not occur for the uncoupled Mn^{II} signals, which appear with similar intensity in the S_2 and S_1 spectra (as they should) at both temperatures, as relaxation rates for this d^5 ion are very low[36]. Comparing with typical 4.2 K ENDOR data for the broad and narrow ML forms from others (Fig. 6A), our spectra remain more resolved than any previously reported. However a clear 'progression' now becomes apparent, with increasing hyperfine resonance structure becoming visible as measured electron $1/T_1$ relaxation rates decrease. We address this in detail within the Discussion section, below.

Data Analysis – Computer Simulation

EPR spectra of tetra-nuclear manganese species can be described by a total spin Hamiltonian involving the sum of the individual spin Hamiltonians for each Mn ion (i, i = 1…4) and the interaction Hamiltonian (Eq. 2).[37,38]

$$\boldsymbol{H_{Tot}} = \sum_i \boldsymbol{H_i} + \sum_{i,j\,i>j} \boldsymbol{H_{ij}} \quad (2a)$$

$$\boldsymbol{H_i} = \boldsymbol{S_i}.\boldsymbol{D_i}.\boldsymbol{S_i} + \beta\,\boldsymbol{S_i}.\boldsymbol{g_i}.\boldsymbol{B} + \boldsymbol{S_i}.\boldsymbol{A_i}.\boldsymbol{I_i} + \boldsymbol{I_i}.\boldsymbol{Q_i}.\boldsymbol{I_i} - g_n\,\beta_n \boldsymbol{B}.\boldsymbol{I_i} \quad (2b)$$

$$\boldsymbol{H_{ij}} = J_{ij}\,\boldsymbol{S_i}.\boldsymbol{S_j} + \boldsymbol{S_{ij}}.\boldsymbol{D_{ij}}.\boldsymbol{S_j} + V_{ij}\,\boldsymbol{S_i} \times \boldsymbol{S_j} \quad (2c)$$

where for each Mn ion $\mathbf{S}_i$ and $\mathbf{I}_i$ are the electron and nuclear spin operators, respectively, $\mathbf{D}_i$ the zero field splitting tensor, $\boldsymbol{g}_i$ and $\boldsymbol{A}_i$ the electron Zeeman and ^{55}Mn hyperfine coupling tensors, respectively, $\boldsymbol{Q}_i$ the quadrupole tensor, g_n the nuclear g-value, β and β_n the Bohr and nuclear magnetons and $\boldsymbol{B}$ the applied magnetic field. The interaction Hamiltonian (H_{ij}, Eq. 2c) accounts for the isotropic ($H_{ex} = -2J_{ij}\,\boldsymbol{S_i}\cdot\boldsymbol{S_j}$), antisymmetric ($H_{as} = V_{ij}\,\boldsymbol{S_i}\,\boldsymbol{x}\,\boldsymbol{S_j}$) and anisotropic exchange (dipole-dipole and spin-orbit coupling, $H_{dd} = \boldsymbol{S_i}\cdot\boldsymbol{D_{ij}}\cdot\boldsymbol{S_j}$) interactions between pairs of manganese centres (i , j). In the strong exchange limit ($|2J| > |D|$ for dominant isotropic exchange couplings (J)), the spin system is best characterized by a total spin operator $S_T = S_1 + S_2 + S_3 + S_4$. With net anti-ferromagnetic coupling (as here), the S_2-state ML CW EPR spectrum arises from an S_T = ½ ground state and the general spin Hamiltonian can be simplified in first order (Eq. 3), enabling the overall g and manganese hyperfine interactions for the S_T = 1/2 manifold to be written as:[39]

$$\boldsymbol{H_S} = \beta\, \boldsymbol{S_T}.\boldsymbol{g_S}.\boldsymbol{B} + \sum_i \boldsymbol{I_i}.\boldsymbol{A_i}.\boldsymbol{S_T} + \sum_i \boldsymbol{I_i}.\boldsymbol{Q_i}.\boldsymbol{I_i} - \sum_i g_n \beta_n \boldsymbol{I_i}.\boldsymbol{B}$$

$$\boldsymbol{g_S} = \textstyle\sum_i \rho_i\, \boldsymbol{g_i} \quad , \quad \boldsymbol{A_i} = \rho_i\, \boldsymbol{A_{i,ion}} \qquad (3)$$

Here ρ_i is the spin projection coefficient of the ion within the S_T = ½ manifold. $\boldsymbol{A}_{i,ion}$ is a hypothetical 'isolated ion' value for the ion in a chemically 'equivalent' environment (ligands etc.). This is in principle obtainable from a single determinant quantum chemical calculation on the geometry optimized tetra-nuclear cluster in the S_2 state. The complexity of the S_2 EPR and ENDOR data seen here means that simple Spin Hamiltonian parameter sets (as previously employed), with all the g, ^{55}Mn hyperfine and quadrupole tensors aligned with modest, at most, anisotropy, are inappropriate. Following inferences drawn above from the ENDOR measurements, we undertook systematic simulations using one large highly anisotropic coupling (Mn1), one medium (of the order of isolated ion values) coupling (Mn2) and two smaller sets of couplings (Mn3,4), corresponding to the ENDOR resonances below 100 MHz (and the resolved 'super-hyperfine' structure in the CW EPR spectra). Such a combination is actually consistent with some previous exchange coupling models [10,15,19], suggesting values of (2, -1, ~0, ~0) for the spin projection coefficients on Mn1..4 (see Discussion). All effective spin Hamiltonian tensors are permitted to be anisotropic and non-aligned, with the molecular axes defined by the principal directions of the largest hyperfine coupling. CW EPR simulations of the S_2 ML signal were performed in EasySpin[29], using the 2nd order perturbation option (4 Mn ions), or full matrix diagonalization (3 Mn ions). Quadrupole interactions were not included, as with previous studies involving > 2 coupled Mn centres.[24] Full matrix diagonalization of the spin Hamiltonian is impractical for four exchange coupled Mn centres. From preliminary calculations on systems with 3 Mn centres, quadrupole terms of the magnitudes here (see below) had little influence on the simulated CW EPR spectra at X band. However they possibly have some effect and studies using the Molecular Sophe[37,38] computer simulation software suite are currently underway. These will be reported separately. Initial estimates of the Mn hyperfine tensors and their orientations within the Mn_3^{III} Mn^{IV} cluster were obtained from DFT calculations on modelled structures.[30,31] Principal components of hyperfine tensors and final adjustment of relative orientations were made manually. Because of the resolution in Fig. 1 (~ 1 mT), we used a 1.5 mT isotropic line width parameter, which is significantly less than that employed by others (generally > 3 mT by our estimates).

Computer simulation of the X-band CW EPR ML spectra (Fig. 1) utilizing the spin Hamiltonian parameters in Table 1, yields the red spectra for the broad and narrow forms (Fig. 7A,B respectively) which reproduce most of the resonances in both cases. Deviations near g = 2 may reflect imperfect subtraction of the strong background features (Tyr_D etc.) in the S_2 –S_1 difference spectra. The broad form simulation shows more fine detail near the spectral edges than seen experimentally and we return to this below. The parameters for Mn1,2 appear robust, from our fitting and those for Mn3 appear to be reasonable, although we have not tried to fit a quadrupole term here, which could be significant

Table 1: CW EPR and ENDOR Simulation Parameters for (A) the 'Broad' and (B) 'Narrow' forms of the S_2 Multiline Signal, from spinach PS II.[a]

A: Broad Form[b]

spin Hamiltonian Interaction	X	Y	Z	Isotropic Value[c]	ρ
g	1.989	2.008	1.964	1.987	-
$\mathbf{A_{Mn1}}$ [c,d]	-668 *(-658)*	-536 *(-534)*	-337 *(-329)*	-514 *(-507)*	≥2.0
$\mathbf{Q_{Mn1}}$ [c]	*(-8)*	*(4.5)*	*(3.5)*	-	-
$\mathbf{A_{Mn2}}$ [c]	185 *(185)*	242 *(242)*	273 *(273)*	233 *(233)*	-1
$\mathbf{A_{Mn3}}$ [c]	-78 *(-78)*	-12 *(-12)*	-46 *(-46)*	-45 *(-45)*	< 0.2
$\mathbf{A_{Mn4}}$ [c]	1*(1)*	20*(15)*	1*(1)*	7*(6)*	<|0.05|
Euler angles[e]	α	β	γ	-	-
$\mathbf{R_{Mn1}}$	0	0	0	-	-
$\mathbf{R_{Mn2}}$	0.422	0.75	-0.737	-	-
$\mathbf{R_{Mn3}}$	-0.135	0.21	0.284	-	-
$\mathbf{R_{Mn4}}$	0	0	0	-	-

B: Narrow Form[f]

spin Hamiltonian Interaction	X	Y	Z	Isotropic Value[c]	ρ
g	1.989	2.008	1.964	1.987	-
$\mathbf{A_{Mn1}}$ [c,d]	-668	-536	-337	-514	≥2.0
$\mathbf{Q_{Mn1}}$ [c]	-	-	-	-	-
$\mathbf{A_{Mn2}}$ [c]	185	242	273	233	-1
$\mathbf{A_{Mn3}}$ [c]	-45	-8	-32	-28	< 0.1
$\mathbf{A_{Mn4}}$ [c]	-	-	-	-	-
Euler angles[e]	α	β	γ	-	-
$\mathbf{R_{Mn1}}$	0	0	0	-	-
$\mathbf{R_{Mn2}}$	0.173	0.35	-0.338		
$\mathbf{R_{Mn3}}$	-0.14	-0.06	-0.08		
$\mathbf{R_{Mn4}}$	-	-	-		

[a] ENDOR parameters in brackets. [b] Isotropic EPR (ENDOR) line width, 1.5 mT (2-3 MHz), ν = 9.3766 GHz, ENDOR static field (*g = 2.05*), Method EPR (ENDOR): 2nd Order Perturbation Theory (Matrix Diagonalization). [c] Units for A and Q, MHz. [d] Total effective values ($\rho \boldsymbol{A}_{ion}$, see text). [e] Units for Euler Angles, radians. [f] Isotropic EPR (ENDOR) line width, 1.5 mT (2-3 MHz), ν = 9.3785 GHz, ENDOR static field (*g = 2.05*), Method: 2nd Order Perturbation Theory.

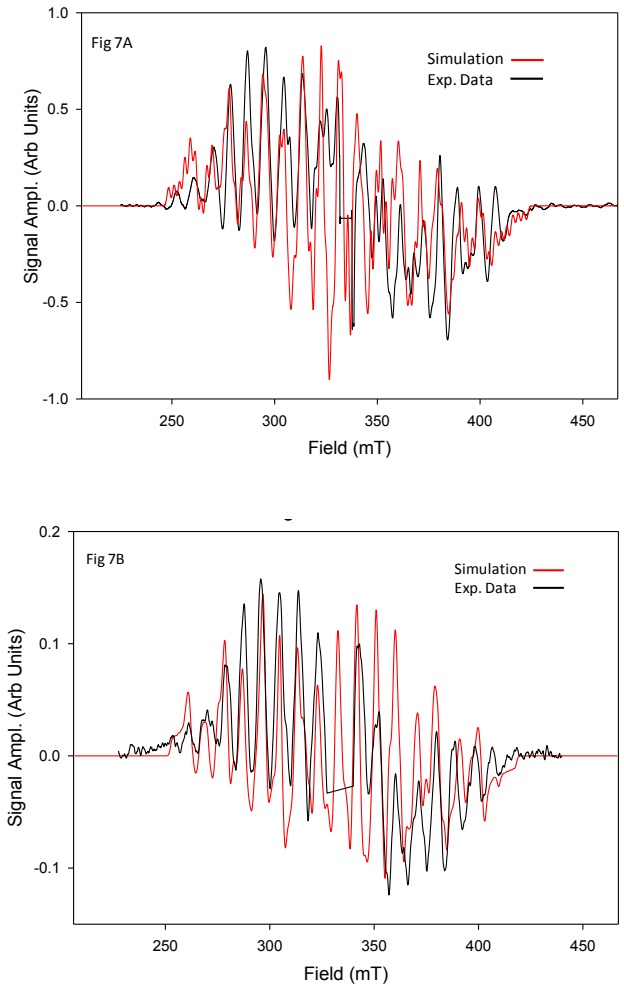

Figure 7. Simulations of the broad form (A) and narrow form (B) S_2 ML CW EPR spectra from Fig. 1, using the parameter values in Table 1 A, B. The regions near g = 2 in the experimental data are distorted (or omitted) due to Tyr_D subtraction artifacts and are not part of the S_2 ML spectra.

since the effective hyperfine tensor is not large. The Mn4 parameters are merely indicative and simulations using Mn1,2,3 only (plus quadrupole for Mn1) give results hardly different from that in Fig 7A (not shown, but Fig 7B has no Mn4 contribution).

Thus Mn4 is virtually 'switched off' while both Mn1 and 3 are highly anisotropic and almost totally rhombic. Even Mn2 (likely oxidation state IV) has significant rhombic anisotropy for such an ion. While the number of free parameters is large, many of these (principal component magnitudes of the ^{55}Mn hyperfine tensors) are constrained by the ENDOR results. The simulations (both CW and ENDOR) are insensitive to the relative signs of $\boldsymbol{A_{Mn3}}$ and $\boldsymbol{A_{Mn4}}$ and those shown are chosen on the basis of PELDOR experiments, described in the Discussion section.

A computer simulation of the X- Band ENDOR spectrum (point b, Fig. 5A), using parameters from Table 1 (ENDOR) is shown in Fig. 8A. This assumes full powder pattern contributions for Mn2,3,4 and an approximate simulation for Mn1 (see below). Relative scaling between these is necessarily arbitrary, that shown is reasonable from the experimental data. They are quantitatively (within ~5 MHz) consistent with the data for

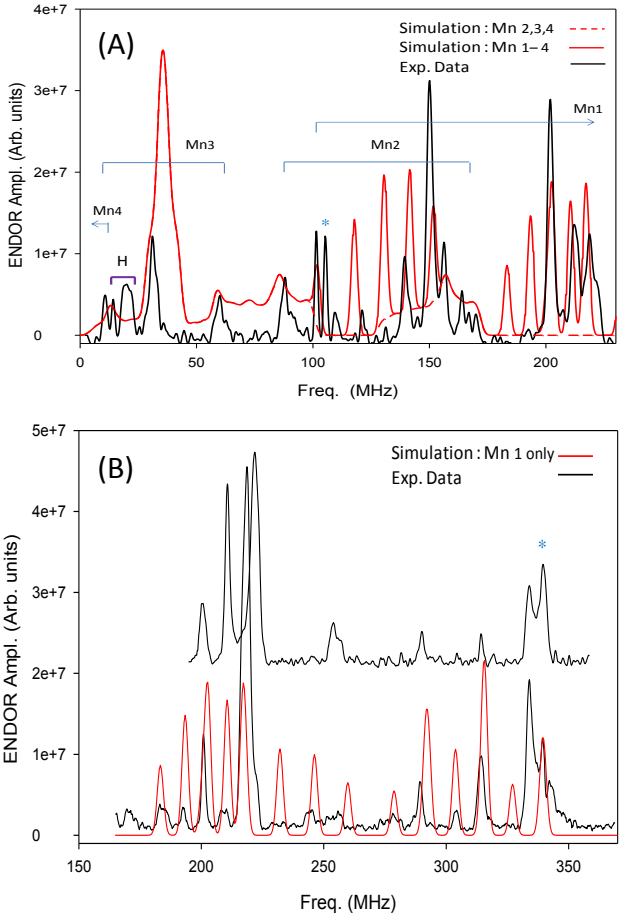

Figure 8: Computer simulation (solid red) of the ^{55}Mn ENDOR spectra (black) of PS II Cores with the spin Hamiltonian parameters listed in Table 1 (ENDOR). (A) Low frequency region of the ENDOR spectrum (Fig. 2, point b). The individual Mn regions have been indicated in the figure. Powder pattern from Mn2,3,4 shown dashed (constitutes a total simulation below 100 MHz). Mn1 contribution orientationally emphasized (see text). (B) High frequency region of the ENDOR spectrum (Fig. 2, point b). Calculation includes only Mn1 and describes the resonances in the region ~ 170 -360 MHz.

frequencies, but intensities are semi-quantitative only. The EasySpin simulation includes the quadrupole interaction, but for randomly oriented systems calculates a powder pattern average of nuclear transitions, assumed uniformly sampled at the field point. This is not the case for the highly resolved, anisotropic spin packets involved here, (particularly for Mn1 contributions, below), but is more reasonable for the weaker couplings (Mn 3,4) when sampling near the centre of the ML EPR spectrum. Strong transitions above 200 MHz arise from Mn1, but this ion also contributes (along A_z manifold) in the ~100 - 150 MHz region.

Given the inferred effective hyperfine coupling for Mn1, whose magnitude and anisotropy is the largest known for a Mn^{III} centre (ESI Fig. S2), a different approach is needed to simulate ENDOR contributions from this centre. At any given field measurement point, all molecular orientations are unlikely to be equally represented in the (narrow) electron spin packets sampled for ENDOR. While rigorous simulation is difficult an approximate approach is possible, consistent with the baseline

data levelling used here. Because the A_1 tensor is near rhombic (i.e. $A_{iso} \sim A_Y$), each principal axis is almost equally likely to be viewed along a given orientation within the powder pattern. We assume the sharp turning points associated with these directions are the prominent features seen in the experimental ENDOR data (particularly the extremes, A_X, A_Z). This is analogous to the well known situation in CW EPR, with narrow intrinsic linewidth and high g anisotropy (e.g. Fe systems). Here only the g tensor turning points are well resolved in the powder pattern, for statistical selection reasons. Since we employed baseline levelling of the raw ENDOR data (ESI, Sections ES4, ES5), those broadened contributions from non principal axis aligned centres would not be reliably preserved in the data analysed.

Given the magnitudes of the other Mn couplings, only ENDOR transitions from $|M_I| = ½$ on the A_X manifold are likely to be seen, for sampling near the ML centre (ESI Section ES3). Transitions from all M_I values on the A_Z manifold should be seen, with some for A_Y (all included for simplicity). Further, the local density of transitions (i.e. likely hood of detection) near the pattern centre should be inversely proportional to the principal axis $A_{1,i}$ value (i = x, y, z) for Mn1 (ESI Fig. S2). Fig. 8B shows such a simulation of the spectra from Fig. 5B (point b), using the Mn1 parameters alone from Table 1. Again, frequencies are in reasonable agreement with the experimental data for most features, but some intensities (notably y direction, ESI Fig. S2) are exaggerated. The intense peaks in the 200-225 MHz region arise from the quadrupole manifold of $A_{1,Z}$ (see also Fig. 8A), variably selected with precise observation point, while those above 300 MHz come mainly from the $A_{1,X}$ manifold. Slightly different values of the Mn1 hyperfine terms are estimated from the CW EPR and ENDOR fits (Table1). We suspect some spread of Mn1 (*Ax* especially) parameters exists in our samples, which would lead to 'blurring' of the fine detail seen in the simulations, but less experimentally, in the CW EPR pattern near the spectral edges (Fig. 7A). Further, we assume alignment of the quadrupole and hyperfine tensors for Mn1 (unlikely for a centre of its unusual nature), which may explain the slight deviations between predicted and observed peak positions. Nonetheless, the above confirms that the intrinsic line broadening in our samples at 2.5 K is small, as the 25 ns microwave pulse inverts electron spin packets that are only ~ 0.4 mT wide. The intensity distribution in the experimental ENDOR spectra suggests pronounced (largely uncontrolled) orientation selection (ESI Fig. S3).

While the anisotropy of the Mn hyperfine parameters in Table 1 is significantly greater than that in dinuclear $Mn^{III,IV}$ model compounds,[12,13] the effective A_{iso} values seen (~ 400-450 MHz for Mn^{III} and ~ 200-240 MHz for Mn^{IV}) are not inconsistent with those in Table 1. The Mn^{III} and Mn^{IV} centres of the model complexes should have (strong coupling) projection coefficients of $\rho_{III} = 2.0$ and $\rho_{IV} = -1.0$ and on this basis the spin projection factors in Table 1are estimated. We return to the anisotropy of the effective hyperfine parameters below (Discussion).

Discussion

Pulsed ENDOR, (e.g. Davies ENDOR) requires the nuclear T_1T_2 product to be sufficiently long for coherent magnetization rotation during the RF pulses.[26] The results here demonstrate the dramatic influence of magnetic relaxation (generally nuclear spin, related to electron spin, below) on detection of ^{55}Mn ENDOR in the OEC. In our data at 4.2 K and in virtually all previous ENDOR studies on the ML system (see Fig. 6A), the ENDOR is dominated by resonances from Mn2, (roughly, the principal axis values listed in Table 1). The repeating envelope structure in the 100-160 MHz region of the broad +EtOH spectrum of Britt et al.,[18a] with peak spacing ~ 14 MHz, is clearly similar to that predicted here for the quadrupole structure on the lower edge of the broad form A_{1z} manifold (ESI Section ES4, spacing ~ 12.5 MHz). This is consistent with our well established observation that the membrane +EtOH ML spectrum is the 'broadest' seen,[5,16] with a quadrupole interaction on Mn1 somewhat larger again than that seen in our PS II core complexes and likely larger than that of the narrow form, which remains yet to be reliably resolved. (but see ESI Section ES6). The narrow form (+MeOH) data[22] seem to reflect principally an envelope from Mn2.

Although further studies are planned, a revealing pattern now emerges. It is well established that electron T_1 relaxation, if too fast, prohibits observation of ^{55}Mn ENDOR in mixed valence model systems.[40] This is particularly true in $Mn^{II,III}$ complexes, for which only one, 'Piv OH', has yielded resolved ENDOR spectra.[40] At 4 K the electron relaxation rate, $1/T_1$, for Piv OH[41] is of the same order (1×10^4 s^{-1}) as that of *all* PS II samples in Fig. 4, except the plant core complexes, whose average rate at 4 K is ~ 250 s^{-1}. For the extensively studied $Mn^{III,IV}$ complexes, which readily yield full range Mn ENDOR spectra,[40] the rate at 4 K is typically ~ 10 s^{-1}.[41] For the broad (+EtOH) form ENDOR spectra of Britt et al. in Fig. 6A, the corresponding electron relaxation rate is ~ 10^3 s^{-1}.[35] Thus a clear phenomenology for Mn ENDOR detection near the pattern envelope peak (necessary for PS II, where effective centre concentrations are 5-10 times less than for model compounds) emerges as:

1. T_1 Rate > 10^4 : No resolved ENDOR spectra (all $Mn^{II,III}$ complexes except Piv OH)
2. T_1 Rate ~10^4 : Only resonances in the region ~ 90-160 MHz from nearly isotropic effective hyperfine tensors are clearly seen ($Mn2^{IV}$ for the OEC, Fig. 6A, Mn^{III} for Piv OH, Fig. 2[40]). Broad resonances from Mn^{II} in Piv OH are seen above 200 MHz. These are probably observable only due to high sample concentration (1 mM) used. Nothing resolved here from OEC.
3. T_1 Rate ~10^3 : Mn2 envelope clearly seen (Fig. 6A),[18a] overlaid now with resolved broad form quadrupole peaks from A_{1z} manifold of Mn1. These probably extend up to ~ 250 MHz at least. Nothing clearly resolved near 300 MHz or above.[18a]
4. T_1 Rate ~250 : Now contributions from Mn1,2,3 are clearly seen, but the Mn2 envelope is most prominent (Fig. 6A). Mn1 resolved quadrupole structure comes mainly from A_{1z} manifold and does not extend beyond 230 MHz (Fig. 6B).
5. T_1 Rate < 100 : Finally full contributions from Mn1,2,3 (at least) are clearly seen in the OEC (Fig. 5A,B). All resonances in $Mn^{IV,III}$ models resolved, for example Cox et al.[40] and references therein.

It is now totally clear why no previous Mn ENDOR studies on the OEC S_2 state ML signal have revealed the range of hyperfine couplings seen here. This follows from the matters alluded to in the Introduction on nuclear relaxation. Sample *nuclear relaxation* conditions, *correlating* generally with electron $1/T_1$ rates < 100 s^{-1} at the measurement temperature, are required. As noted the relevant nuclear rates are the dephasing rates (in the rotating frame, basically T_2 processes), which suppress the ENDOR. These effective T_2 rates can of course be much greater than T_1 rates, as they are strongly influenced by low frequency phonon modes, which generally dominate at low temperatures[36]. However, the Electron T_1 rates are readily measured and serve as a convenient 'proxy indicator' for magnetic relaxation rates generally. Further, the Mn oxidation state itself likely plays a role. Mn^{III} ions, which often have readily distortable Jahn-Teller axes (as for Mn1,3,4 in our recent OEC modelling studies[30]) will generally experience significant phonon induced electron/nuclear hyperfine modulation, thus driving nuclear relaxation rates[49]. It is thus unremarkable that generally, *only* the ENDOR resonances arising from Mn2, which is in the IV oxidation state (uniquely in the low paradigm), are readily seen at 4.2 K. Following the initial studies of Britt et al.[18a] (+EtOH samples), *all* subsequent studies up till the present involved PS II material with electron spin relaxation rates, $1/T_1$ at least two orders of magnitude faster than those seen here (~ 10^2). Essentially only Mn2 resonances were reliably seen. Based on extrapolations of data in Fig. 4, measurement temperatures of 2 K or lower would be needed with conventional PS II samples for full ENDOR development, however our active core material allows this to be raised to ~3 K.

Our results also have significant implications for the redox organization of the Mn ions within the S_2 state of the OEC cluster. The observation of large fractional anisotropy on two, probably three Mn centres, with modest anisotropy in the remaining centre (near rhombic in all cases), suggests that three Mn^{III} ions and one Mn^{IV} ion are present, i.e. the low oxidation state paradigm. We have shown computationally[42] that Mn X-ray Absorption Near Edge Structure (XANES) data are consistent with this, as are other spectroscopic results[10] and the Mn oxidation states inferred from photo-assembly experiments.[43] Finally, a very recent large scale computational study of the OEC region[44] rationalized both the 2.9 Å and 1.9 Å XRD structures,[3,4] within the low oxidation state paradigm, without invoking radiation damage or photo-reduction.

Another remarkable result is that the magnetic coupling in S_2 is 'dimer like' (spin projections $\rho_1 \sim 2$ and $\rho_2 \sim -1$ for Mn1,2) with two Mn ions (Mn3,4) almost 'switched off' (net spin $\rho_3, \rho_4 \sim 0$). This has been proposed empirically[5] and as mentioned above, is consistent with or admitted as one possibility within earlier magnetic exchange coupling models [10,15,19] of the OEC. The failure to realize this before, by detection of ENDOR resonances outside the ~ 70-170 MHz region, is a direct consequence of nuclear relaxation effects, fully overcome for the first time here. Our results allow rationalization of a number of earlier experiments, now interpretable as probing spin projections on the individual Mn of the OEC directly[30]. Firstly, ESEEM/ENDOR determinations show that the effective $|A_{iso}|$ of the single strong ^{14}N coupling in the S_2 ML signal (from Nτ of His332 to Mn1), is ~ 6-7 MHz.[45,46] This occurs only through π interactions,[10] for which the 'isolated ion' ^{14}N $|A_{iso}|$ is ~ 2-4 MHz.[45,46] So ρ_1 must be ~ 2, as found here. Similarly, Britt et al. showed from ^{13}C terminal labelling of the D1 peptide that the ρ value of Mn2 was most likely -1.[47] (see also[30]) The same group[48] also showed that the fully functional His mutant at the D1 Asp170 position (ligates Mn4) showed *no* extra detectable ^{14}N coupling in S_2. This was very surprising, but is now easily understood given our result that $\rho_4 \sim 0$. Similarly, the recent W-band studies of Lubitz et al.,[46] together with the results here, yield a totally consistent molecular model of the OEC S_2 state and locate one substrate water molecule and our molecular axis frame within it (Fig. 9 below). Further, the very recent PELDOR studies of Mino et al.,[49] exploring the through space dipole/dipole interaction between the stable Tyr_D radical (~ 30 Å from the OEC cluster) and the S_2 ML spin ½ centre, found a best match to their data assuming $\rho_1 \sim 2.0$ and $\rho_2 \sim -1.2$, with ρ_3, ρ_4 values such that $\rho_3 + \rho_4 \sim 0.2$. This is also quite consistent with the results obtained here.

Finally, the hyperfine parameters assigned here to Mn1 are notable, by comparison with those for Mn^{III} centres in model $Mn^{III,IV}$ complexes and super-oxidised catalase (probably the closest protein analogue). Lubitz, Bittl et al. report extensive data on such systems[13]. The Mn1 maximum hyperfine component is ~ 660 MHz and the total anisotropic range, ~ 330 MHz. The Mn hyperfine tensor is almost totally rhombic and the fractional anisotropy is ~ 65% of the A_{iso} value. For the variety of model systems, the hyperfine symmetry of the Mn^{III} centre ranges from near axial, to moderately rhombic, with a maximum fractional anisotropy of ~ 45% of A_{iso} and maximal hyperfine component of ~ 500 MHz (but not both for the same compound). A structural comparison of the model systems in ref 13 (including catalase) with the OEC (Fig 9) shows that the OEC has the lowest (C_1) symmetry of any and that, unlike the model complexes, *all* Mn centres we assign to the Mn^{III} state (Mn1,3,4) are essentially five co-ordinate (vs. six co-ordinate in model complexes). This is because the O(5) species is at least ~ 2.5Å from any of these Mn^{III} ions, presumably along the Jahn-Teller axes[44]. The possible consequences of these and other factors for the hyperfine interactions are presently under computational study.

Model of the OEC S_2 State from this work and other EPR/Theoretical studies

The magnetic/electronic structure of the OEC in the S_2 state, which emerges from these considerations, is summarised in Fig. 9. Magnetically it is not too far removed from a simple model in which a strongly anti-ferromagnetically coupled spin 1/2 $Mn^{III,IV}$ dimer (Mn1,2) is closely adjacent to, but only weakly exchange coupled with, an equi-valent Mn dimer (Mn3,4, probably $Mn^{III,III}$), whose internal coupling is also anti-ferromagnetic. The latter pair has zero net spin ground state but can thermally access excited states of even spin (Orbach like process), which would be powerful paramagnetic relaxation enhancers through dipole-dipole interactions. Thus the good fit of the mixed dipolar model to the ML relaxation in Fig. 3 is not surprising, particularly as the F parameter increases with temperature.

The conclusion that the magnetic coupling in the S_2 OEC is nearly 'dimer of dimers', with $\rho_1 \sim 2.0$, $\rho_2 \sim -1$, and ρ_3, ρ_4 being of opposite sign and small in magnitude (near cancelling) is superficially odd given the Mn cluster geometry. However, it is totally consistent with what are the most advanced (and recent)

quantum chemical calculations yet undertaken on OEC models. These[19] are the first such treatments beyond conventional density functional theory (DFT) and use density matrix renormalisation group theory (DMRG), generating near exact many electron wave function solutions ('entangled states'). A robust conclusion from these, even in an assumed high oxidation state paradigm, was that ρ_1 = 2.0, ρ_2 = -1.0 and, and ρ_3, ρ_4 were each of small, equal magnitude and opposite sign (~ 0.2 to 0.3 magnitude). Because the *total* ML pattern width is ~ 5.5 GHz, and the dominant line spacing is ~ 250 MHz (ie 9.0 mT), these calculations essentially *demand* that one coupling be large, i.e. of order 600 MHz, since two Mn couplings are small. This arises because, in simple terms,

$$\text{ML width (5.5 GHz)} \sim 5(A_{1\,\text{eff}} + A_{2\,\text{eff}} + A_{3\,\text{eff}} + A_{4\,\text{eff}}) \quad (4)$$

where the $A_{i,\text{eff}}$ terms are appropriate (~ angularly averaged) effective ^{55}Mn hyperfine magnitudes. One, ($A_{2\,\text{eff}}$, say) must be ~ 250 MHz (observed), two ($A_{3,4\text{eff}}$, say) are 'small' (< 70 Mhz, quantum computational[19] and seen here, Fig 1A). So $A_{1\,\text{eff}}$ is at least as stated above (600 MHz) and indeed as also seen here.

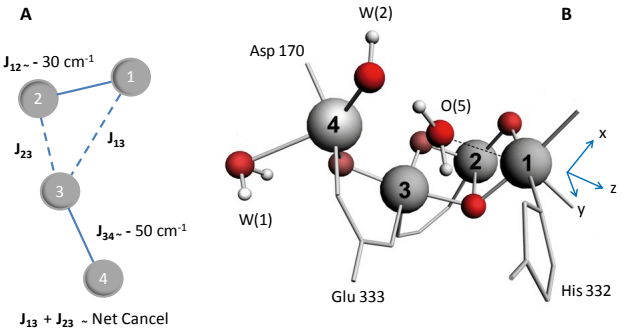

Figure 9. Geometric and electronic structures of the OEC. (A). Magnetic coupling scheme for the S_2 OEC, based on DFT calculations of model OEC clusters,[10] which would be consistent with the EPR studies on the S_2 ML state reported here. Mn numbered by our usual convention.[30] Small values or near net cancellation of the J_{23} and J_{13} terms would need to occur. Very recent 'entangled state' quantum calculations support this[19] Then the system approximates two isolated dimers, one with net spin ½ ($Mn^{III,IV}$ dimer (Mn1,2)) and the other with net spin ~ 0 ground state ($Mn^{III,III}$ dimer (Mn3,4)). (B) Structural model of the OEC (S_2 state), based on the 1.9 Å XRD structure of Kamiya, Shen et al.[3] and our recent computational modeling of this structure.[44] The O(5) species has been identified as a water molecule,[44] as is the W1 species, but W2 is likely an hydroxide in S_2.[31] The molecular axis system, consistent with our data and that of Lubitz, Cox et al.[46] is shown. This has a z axis essentially along the Mn1 – O(5) direction. The y axis points along the Mn1 - N(His 332) direction.

Conclusions

In conclusion, we have presented the first ^{55}Mn pulsed ENDOR studies on the S_2 state multiline spin ½ centre of the OEC in PS II core complexes at temperatures down to 2.5 K. The longer electron/nuclear spin relaxation times found at 2.5 K, have allowed us to observe highly resolved ^{55}Mn ENDOR resonances of the S_2 state of the OEC at frequencies beyond those observed previously. ^{55}Mn ENDOR hyperfine couplings ranging from ~ 50 to ~ 680 MHz were observed for the S_2 state multiline EPR signal. In conjunction with complementary high resolution X-Band CW EPR measurements and detailed computer simulations, the data reveal that at least two and probably three Mn hyperfine couplings with large anisotropy are observed, indicating that three Mn^{III} ions are likely present in the functional S_2 state of the enzyme. This suggests that the low oxidation state paradigm obtains for the OEC, with mean Mn oxidation levels of 3.0 and 3.25 in the S_1 and S_2 states respectively. An unexpected Mn exchange coupling exists in the S_2 state, with two Mn ions nearly magnetically silent, in agreement with very recent high level quantum computational studies (DMRG) of the OEC electronic states[19]. Our results allow a systematic rationalization of a number of previous ligand ESEEM/ENDOR studies on the OEC, some previously puzzling. This yields a common picture which is closely consistent with recent photo-assembly[43] and large scale structural modelling of the OEC.[44] using DFT

Acknowledgements

The authors gratefully acknowledge financial assistance from the Australian Research Council and access to the Australian National University supercomputer facilities of the National Computational Infrastructure. We also thank Dr. N. Cox for help with installing EasySpin at ANU.

Notes and references

[a] *Research School of Chemistry, Australian National University, Canberra, ACT 0200, Australia. Fax: +61-2-6125-0750; Tel: +61-2-6125-4546; E-mail: Ron.Pace@anu.edu.au*
[b] *Centre for Advanced Imaging, The University of Queensland, Brisbane, Queensland, 4072, Australia. Fax: +61-7-3365-3833; Tel: +61-7-3365-3242; E-mail: Graeme.Hanson@cai.uq.edu.au*

† Electronic Supplementary Information (ESI) available: Section ES1: Dipolar Relaxation Model, Section ES2: ENDOR Sampling Point Sensitivity, Section ES3: S2 ML Envelope Shapes for Mn1 Principal Axis Directions, Section ES4: Origins of Simulated ENDOR Transitions, Section ES5: Baseline Uncorrected ENDOR data and EASYSPIN Powder Simulation, Section ES6: Model of the OEC S2 State from this Work and other EPR studies. See DOI: 10.1039/b000000x/

‡ Abbreviations. CW, Continuous Wave; Chl., Chlorophyll; DFT, Density Functional Theory; (DMRG) Density Matrix Renormalisation Group Theory ESE, Electron Spin Echo; ENDOR, Electron Nuclear Double Resonance; ESEEM, Electron Spin Echo Envelope Modulation; EtOH, Ethanol; MeOH, Methanol; ML, Multiline; OEC, Oxygen Evolving Complex; OD, Optical Density; PpBQ, p-Phenylbenzo-quinone; PS, Photosystem; XANES, X-ray Absorption Near Edge Structure; XRD, X- Ray Diffraction. PELDOR, pulsed electron-electron double resonance.

†† There is one report in the public domain from the Lubitz, Bittl group (then at the Technical University, Berlin) of ^{55}Mn ENDOR couplings in the range ~ 550-600 MHz, reproducibly observed on the S_2 ML EPR spectrum from spinach PS II membrane particles: M. Kammel, PhD Thesis: Faculty of Mathematics and Science, Technical University, Berlin, 2003.

§ An excellent example of this can be found in another thesis from the Lubitz, Bittl group (Technical University, Berlin) K.-O. Schäfer, PhD Thesis, Faculty of Mathematics and Science, Technical University, Berlin, 2002. An example of Mn^{II}-Mn^{III} system has also been reported by Cox et al.[24]

1. K. Satoh, T. J. Wydrzynski and Govindjee in *Photosystem II: The Light Driven Water: Plastoquinone Oxidoreductase*, ed. T. J.

Wydrzynski, K. Satoh and J. A. Freeman, Springer, Dordrecht, The Netherlands, 2005, pp. 11-22.
2. W. Hillier and T. J. Wydrzynski, *Biochim. Biophys. Acta*, 2001, **1503**, 197-209.
3. Y. Umena, K. Kawakami, J.-R. Shen and N. Kamiya, *Nature*, 2011, **473**, 55-60.
4. a) J. Guskov, A. Kern, M. Gabdulkhakov, M. Broser, A. Zouni and W. Saenger, *Nature Struct. Mol Biol.*, 2009, **16**, 334-342., b) B. Loll, J. Kern, W. Saenger, A. Zouni, J. Biesiadka, *Nature* 2005, **438**, 1040-1044, c) K. N. Ferreira, T. M. Iverson, K. Maghlaoui, J. Barber, S. Iwata, *Science (Washington, DC, United States)* 2004, **303**, 1831-1838, d) N. Kamiya, J.-R. Shen*, Proc. Natl. Acad. Sci. USA* 2003, **100,** 98-103, e) A. Zouni, H.-T. Witt, J. Kern, P. Fromme, N. Krauss, W. Sänger, P. Orth, *Nature,* 2001, **409**, 739.-743.
5. K. A. Åhrling, R. J. Pace and M. C. W. Evans in *Photosystem II: The Light Driven Water: Plastoquinone Oxidoreductase*, ed. T. J. Wydrzynski, K. Satoh and J. A. Freeman, Springer, Dordrecht, The Netherlands, 2005, pp 285-306.
6. G. C. Dismukes and Y. Siderer, *Proc. Natl. Acad. Sci. U.S.A.*, 1981, **78**, 274-278.
7. J. Dasgupta, G.M. Ananyev and G. C. Dismukes, *Coord. Chem. Rev.*, 2008, **252**, 347-360.
8. V. K. Yachandra, K. Sauer and M.P. Klein, *Chem. Rev.*, 1996, **96**, 2927-2950.
9. M. Haumann, C. Müller, P. Liebisch, L. Iuzzolino, J. Dittmer, M. Grabolle, T. Neisius, W. Meyer-Klaucke and H. Dau, *Biochemistry*, 2005, **44**, 1894-1908.
10. P. Gatt, R. Stranger and R. J. Pace, *J. Photochem. Photobiol. B*, 2011, **104**, 80-93.
11. R. J. Pace, L. Jin and R. Stranger, *Dalton Trans.*, 2012, **41**, 11145-11160.
12. S. R. Cooper and M. Calvin, *J. Am. Chem. Soc.*, 1977, **99**, 6623-6630.
13. K.-O. Schäfer, R. Bittl, F. Lendzian, V. Barynin, T. Weyhermüller, K. Wieghardt and W. Lubitz, *J. Phys. Chem. B*, 2003 **107**, 1242-1250.
14. G. Blondin, R. Davydov, C. Philouze, M.-F. Charlot, S. Styring, B. Åkermark, J.-J. Girerd and A. Boussac, *J. Chem. Soc., Dalton Trans.*, 1997, 4069-4074.
15. T. G. Carell, A. M. Tyryshkin and G. C. Dismukes, *J. Biol. Inorg. Chem.*, 2002, **7**, 2-22.
16. K. A. Åhrling and R. J. Pace, *Biophys. J.*, 1995, **68**, 2081-2090.
17. J. Bonvoisin, G. Blondin, J.-J. Girerd and J.-L. Zimmermann, *Biophys. J.*, 1992, **61**, 1076-1086.
18. D. W. Randall, B. E. Sturgeon, J. A. Ball, G.A. Lorigan, M. K. Chan, M. P. Klein, W. H. Armstrong and R. D. Britt, *J. Am. Chem. Soc.*, 1995, **117**, 11780-11789, b) J. M. Peloquin, K. A. Campbell, D. W. Randall, M.A. Evanchik, V.L. Pecoraro, W. H. Armstrong and R. D. Britt, *J. Am. Chem. Soc.* 2000**,** ***122,*** 10926-10942
19. Y. Kurashige, G. K.-L. Chan and T. Yanai, *Nature Chem.*, 2013, **5**, 660-666
20. C. Teutloff, S. Pudollek, S. Keßen, M. Broser, A. Zouni and R. Bittl, *Phys. Chem. Chem. Phys.*, 2009, **11**, 6715-6726.
21. S. Pudollek, F. Lendzian and R. Bittl*, Biochem. Soc. Trans.*, 2008, **36**, 1001-1004.
22. L. V. Kulik, B. Epel, W. Lubitz and J. Messinger, *J. Am. Chem. Soc.*, 2007, **129**, 13421-13435.
23. N. Cox, L. Rapatskiy, J. H. Su, D. A. Pantazis, M. Sugiura, L. Kulik, P. Dorlet, A. W. Rutherford, F. Neese, A. Boussac, W. Lubitz and J. Messinger, *J. Am. Chem. Soc.*, 2011, **133**, 3635-3648.
24. J. H. Su, N. Cox, W. Ames, D. A. Pantazis, L. Rapatskiy, T. Lohmiller, L. V. Kulik, P. Dorlet, A. W. Rutherford, F. Neese, A. Boussac, W. Lubitz and J. Messinger, *Biochim. Biophys. Acta*, 2011, **1807**, 829-840.
25. J. M. Pelloquin, K. A. Campbell, D. W. Randall, M. A. Evanchik, V. L. Pecoraro, W. H. Armstrong and R. D. Britt, *J. Am. Chem. Soc.*, 2000, **122**, 10926-10942.
26. Schweiger and G. Jeschke, *Principles of Pulse Electron Paramagnetic Resonance,* Oxford University Press, Oxford, United Kingdom, 2001, pp 359-403.
27. P. J. Smith, S. Peterson, V. Masters, T. J. Wydrzynski, S. Styring, E. Krausz and R. J. Pace, *Biochemistry*, 2002, **41**, 1981-1989.
28. J. L. Hughes, P. J. Smith, R. J. Pace and E. Krausz, *Biochim. Biophys. Acta*, 2006, **1757**, 841-851.
29. S. Stoll and A. Schweiger, *J. Magn. Reson.*, 2006, **178**, 42-55.
30. S. Petrie, R. Stranger and R. J. Pace, *Chem. Eur. J.*, 2010, **16**, 14026-14042.
31. R. J. Pace, R. Stranger and S. Petrie, *Dalton Trans.*, 2012, **41**, 7179-7189.
32. K. A. Åhrling, M. C. W. Evans, J. H. A. Nugent and R. J. Pace, *Biochim. Biophys. Acta*, 2004, **1656**, 66-77.
33. K. A. Åhrling, M. C. W. Evans, J. H. A. Nugent, R. J. Ball, and R. J. Pace, *Biochemistry*, 2006, **45**, 7069-7082.
34. K. V. Narasimhulu, R. Carmieli and D. Goldfarb, *J. Am. Chem. Soc.*, 2007, **129**, 5391-5402.
35. G. A. Lorigan and D. R. Britt, *Biochemistry*, 1994, **33**, 12072-12076.
36. C. P. Poole and H. C. Farach *Relaxation in Magnetic Resonance* Academic Press, Ney York and London, 1971, Chapt 8- 11
37. G. R. Hanson, C. J. Noble and S. Benson in *EPR of Free Radicals in Solids: Trends in Methods and Applications (2nd Edition)*, ed. A. Lund and M. Shiotani, *Progress in Theoretical Chemistry and Physics,* J. Maruani and S. Wilson, series ed., Springer, Heidelberg, Germany, 2013, **A24**, 223-283.
38. G. R. Hanson, C. J. Noble and S. Benson in *High Resolution EPR: Applications to Metalloenzymes and Metals in Medicine, Biological Magnetic Resonance*, ed. G. R. Hanson and L. J. Berliner, Springer, Heidelberg, Germany, 2009, **28**, 105-173.
39. A. Bencini and D. Gatteschi in *Electron Paramagnetic Resonance of Exchange Coupled Systems*, Springer-Verlag, New York, USA, 1990, pp 48-85.
40. N. Cox, W. Ames, B. Epel, L. V. Kulik, L. Rapatskiy, F. Neese, J. Messinger, K. Wieghardt and W. Lubitz, *Inorg. Chem.*, 2011, **50**, 8238-8251.
41. L. V. Kulik, W. Lubitz and J. Messinger, *Biochemistry*, 2005, **44**, 9368-9374.
42. R. Jaszewski, S. Petrie, R. J. Pace and R. Stranger, *Chem. Eur. J.*, 2011, ***1***7, 5699-5713.
43. D. R. J. Kolling, N. Cox, G.M. Ananyev, R. J. Pace and G. C. Dismukes, *Biophys. J.*, 2012, **103**, 313-322.
44. P. Gatt, S. Petrie, R. Stranger and R. J. Pace, *Angew. Chem. Int. Ed.*, 2012, **51**, 12025-12028.
45. G. J. Yeagle, M. L. Gilchrist Jr., L. M. Walker, R. J. Debus and R. D. Britt, *Phil. Trans. R. Soc. B*, 2008, **363**, 1157-1166.
46. L. Rapatskiy, N. Cox, A. Savitsky, W. M. Ames, J. Sander, M. M. Nowaczyk, M. Rögner, A. Boussac, F. Neese, J. Messinger and W. Lubitz, *J. Am. Chem. Soc.*, 2012, **134**, 16619-16634.
47. J. A. Stull, T. A. Stich, R. J. Service, R. J. Debus, S. K. Mandal, W. H. Armstrong and R. D. Britt, *J. Am. Chem. Soc.*, 2010, **132**, 446-447.
48. T. A. Stich, G. J. Yeagle, R. J. Service, R. J. Debus and R. D. Britt, *Biochemistry*, 2011, **50**, 7390-7404.
49. M. Asada, H. Nagashima, F. H. M. Koua, J.-R. Shen, A. Kawamori and H. Mino, *Biochim. Biophys. Acta*, 2011, **1827**, 438–445.